

Mid-infrared extinction curve for protostellar envelopes from JWST-detected embedded jet emission: the case of TMC1A

K. D. Assani^{1,2}, Z.-Y. Li^{1,2}, J. P. Ramsey³, Ł. Tychoniec^{4,5}, L. Francis⁴, V. J. M. Le Gouellec^{6,7}, A. Caratti o Garatti⁸, T. Giannini⁸, M. McClure⁴, P. Bjerkeli⁹, H. Calcutt⁹, H. Beuther¹⁰, R. Devaraj¹¹, X. Liu⁵, A. Plunkett¹², M. G. Navarro⁶, E. F. van Dishoeck⁴, and D. Harsono¹³

¹ Department of Astronomy, University of Virginia, Charlottesville, VA 22903, USA

² Virginia Institute of Theoretical Astronomy, University of Virginia, Charlottesville, VA 22903, USA

³ Bluedrop Training & Simulation, Inc., 36 Solutions Drive #300, Halifax, Nova Scotia B3S 1N2, Canada

⁴ Leiden Observatory, Leiden University, PO Box 9513, 2300RA, Leiden, The Netherlands

⁵ European Southern Observatory, Karl-Schwarzschild-Strasse 2, 85748 Garching bei München, Germany

⁶ Institut de Ciències de l'Espai (ICE-CSIC), Campus UAB, Can Magrans S/N, E-08193 Cerdanyola del Vallès, Catalonia, Spain

⁷ Institut d'Estudis Espacials de Catalunya (IEEC), c/Gran Capita, 2-4, E-08034 Barcelona, Catalonia, Spain

⁸ INAF-Osservatorio Astronomico di Capodimonte, Salita Moirariello 16, 80131 Napoli, Italy

⁹ Chalmers University of Technology, Department of Space, Earth and Environment, 412 96 Gothenburg, Sweden

¹⁰ Max-Planck-Institut für Astronomie, Königstuhl 17, 69117 Heidelberg, Germany

¹¹ Dublin Institute for Advanced Studies, DIAS Headquarters, 10 Burlington Road, D04C932 Dublin, Ireland

¹² National Radio Astronomy Observatory, 520 Edgemont Road, Charlottesville, VA 22903, USA

¹³ Institute of Astronomy, Department of Physics, National Tsing Hua University, Hsinchu, Taiwan

April 4, 2025

ABSTRACT

Context. Dust grains are fundamental components of the interstellar medium and play a crucial role in star formation, serving as catalysts for chemical reactions and the building blocks of planets. Extinction curves serve as a tool for characterizing dust properties, yet mid-infrared (MIR) extinction remains less constrained in protostellar environments. Gas-phase line ratios from embedded protostellar jets offer a spatially resolved method to measure extinction from protostellar envelopes, complementing traditional background starlight techniques.

Aims. We aim to derive mid-IR extinction curves along the lines of sight toward a protostellar jet embedded within an envelope and assess whether they differ from those inferred in dense molecular clouds.

Methods. We analyze JWST NIRSpec IFU and MIRI MRS observations, focusing on four locations along the blue-shifted TMC1A jet. After extracting observed [Fe II] line intensities, we model intrinsic line ratios using the Cloudy spectral synthesis code across a range of electron densities and temperatures. By comparing observed near-IR (NIR) and MIR line ratios to Cloudy-predicted intrinsic ratios, we infer the relative extinction between NIR and MIR wavelengths.

Results. Electron densities (n_e) derived from NIR [Fe II] lines range from $\sim 5 \times 10^4$ to $\sim 5 \times 10^3 \text{ cm}^{-3}$ along the jet axis at scales $\lesssim 350$ AU, serving as reference points for comparing relative NIR and MIR extinction. The derived MIR extinction values exhibit higher reddening than the empirical dark cloud curve from McClure (2009) at the corresponding n_e and temperatures ranging from a few 10^3 K to $\sim 10^4$ K, as adopted from shock models. While both electron density and temperature influence the NIR-to-MIR [Fe II] line ratios, the ratios are more strongly dependent on n_e over the adopted range. If the MIR emission originates from gas that is less dense and cooler than the NIR-emitting region, the inferred extinction curves remain consistent with background star-derived values.

Conclusions. This study introduces a new line-based method for deriving spatially resolved MIR extinction curves towards embedded protostellar sources exhibiting a bright [Fe II] jet. The results suggest that protostellar envelopes may contain dust with a modified grain size distribution—such as an increased fraction of larger grains, potentially due to grain growth—if the MIR and NIR lines originate from similar grains along the same sightlines. Alternatively, if the grain size distribution has not changed (i.e., no grain growth), the MIR lines may trace cooler, less dense gas than the NIR lines along the same sightlines. This method provides a novel approach for studying dust properties in star-forming regions and can be extended to other protostellar systems to refine extinction models in embedded environments.

1. Introduction

Despite the dust-to-gas mass ratio of 0.01, dust grains are fundamental components of the interstellar medium (ISM), produced during the final stages of stellar evolution and subsequently processed in interstellar environments. These grains act as catalysts for chemical reactions, enabling the formation of complex organic molecules and facilitating key processes essential to star and planet formation (e.g., Johansen et al. 2014; Brügger et al. 2020; Johansen et al. 2021; Boogert et al. 2015; McClure et al. 2023). The earliest stages of planet formation begin with

the growth of dust grains, a process that appears to commence early in the star formation sequence (e.g., Drażkowska et al. 2023). While JWST is beginning to unravel dust grain properties through infrared observations along various lines of sight within molecular clouds (e.g., Declair et al. 2025), it remains less clear how these dust properties persist as a protostar forms and creates a dense environment within a collapsing cloud.

At millimeter wavelengths, low spectral index values—referring to the shallow slope of flux density across the mm regime—are often interpreted as evidence for grain growth, suggesting the presence of large grains in the disks and infalling

envelopes of the youngest protostars (ages $\sim 10^{4-5}$ years) (e.g., Miotello et al. 2014; Galametz et al. 2019; Cacciapuoti et al. 2024). While the sizes of dust grains contributing to low dust emissivities remain less well constrained, models of dust polarization based on radiative alignment torques (RATs) require grains larger than $\sim 10 \mu\text{m}$ to explain observed polarization levels in protostellar envelopes at millimeter wavelengths (Valdivia et al. 2019; Le Gouellec et al. 2019).

Across infrared (IR) to ultraviolet (UV) wavelengths, dust grain properties are typically inferred from extinction curves and/or solid-state features of the refractories and/or volatiles. Extinction curves describe how dust grains absorb and scatter light as a function of wavelength, providing a critical tool for probing their composition, size distribution, and processing in astrophysical environments. Observationally, extinction curves are usually derived by measuring the attenuation of stellar photospheric continuum emission along different lines of sight, revealing how dust interacts with radiation in various astrophysical environments (e.g., Cardelli et al. 1989; McClure 2009; Gordon et al. 2023). Theoretically, extinction models connect these observational trends to underlying dust grain populations by adjusting grain size distributions and compositions to match the observed extinction laws (e.g., Weingartner & Draine 2001; Crapsi et al. 2008; Pontoppidan et al. 2024).

Cardelli et al. (1989) introduced a widely adopted UV to near-infrared (NIR) extinction law derived from line-of-sight observations of bright stars with known spectral types, showing that the shape of the extinction curve depends on the total-to-selective extinction ratio ($R_V = A_V/E(B - V)$), where A_V is the total extinction in the V-band and $E(B - V)$ represents the difference in extinction between the B and V bands. Notably, the observed extinction curves revealed that extinction in the NIR ($\lambda \sim 1 - 5 \mu\text{m}$) appears independent of R_V while a larger dependence is found in UV (the "Far-UV rise"). In the mid-infrared (MIR), McClure (2009) analyzed 5–20 μm Spitzer IRS spectra of background G0–M4 III stars and confirmed that extinction curves derived from stars behind dense dark clouds exhibit higher levels of mid-IR extinction compared to those behind less opaque clouds, which resemble the diffuse interstellar medium (ISM). The higher extinction regimes correspond to flatter MIR extinction curves relative to the NIR that aligns closely with the $R_V = 5.5$, case B, curve in Weingartner & Draine (2001).

From a modeling perspective, the observed extinction differences relative to optical/IR across lines of sight in the UV ($\lambda < 0.16 \mu\text{m}$) and the mid-infrared (5–30 μm) correspond to differences in dust composition, grain size distributions, and the presence of solid-state features such as refractories and volatiles. The $R_V = 5.5$ curve (Case B in Weingartner & Draine 2001) shows higher extinction at $\lambda > 2 \mu\text{m}$ compared to the $R_V = 3.1$ case, attributed to a decrease in small grains ($< 0.1 \mu\text{m}$) and an increased fraction of larger silicate and carbonaceous grains, resulting in the observed flattening of the extinction curve in the MIR relative to the NIR. This flattening effect is also consistent with the "KP5" extinction curve, which models extinction as a function of wavelength for dense clouds and protostellar envelopes, including the effects from ices (e.g., H_2O , CO, and CO_2) that introduce sharp opacity features at specific mid-infrared wavelengths (Crapsi et al. 2008; Pontoppidan et al. 2024). The KP5 model assumes a grain size distribution predominantly larger than $0.1 \mu\text{m}$, with an upper size limit of $7 \mu\text{m}$, consistent with the grain size distribution from Weingartner & Draine (2001) and broadly consistent with that measured for two lines of sight within a dense molecular cloud by Dartois et al.

(2024) using radiative transfer modeling of the scattering wings of ice features towards two background stars in Chameleon I.

With the empirically derived MIR extinction curve from McClure (2009) showing that denser lines of sight ($A_K > 1$) align more closely with the $R_V = 5.5$ Case B curve while more diffuse sightlines ($A_K < 1$) resemble the $R_V = 3.1$ curve, there is growing evidence that dust grains grow larger in denser regions. Extending this trend, should we expect an even flatter MIR extinction curve in the denser regions ($A_K \gtrsim 2$) surrounding a protostar—such as its envelope or disk—where grain size distributions (e.g., due to grain growth) may differ from those inferred in molecular clouds?

One way to probe MIR extinction toward embedded environments is through protostellar outflows, which emit strong atomic and molecular lines that become attenuated by the surrounding dust. Unlike background starlight methods, which require bright sources behind dusty regions, gas emission lines provide a spatially resolved approach to measuring extinction within the envelope itself. These outflows exhibit a hierarchical arrangement of nested structures, commonly traced by species such as [Fe II], H_2 , and CO, distinguishing between collimated jets, wider molecular outflows, and intermediate-angle disk winds (e.g., Harsono et al. 2023; Pascucci et al. 2024; Tychoniec et al. 2024; Delabrosse et al. 2024b; Caratti o Garatti et al. 2024; Le Gouellec et al. 2024b).

Gas emission lines from protostellar jets are produced from radiative shocks, where supersonic outflows collide with more slowly moving material, creating sharp transitions at the shock front (e.g., Frank et al. 2014). At this interface, gas is rapidly compressed and heated, initiating a post-shock cooling zone where atomic and molecular species become emissive (e.g., Hollenbach & McKee 1989). For the NIR and MIR [Fe II] lines, shock models predict that these lines become emissive at electron densities $\sim 10^3\text{--}10^5 \text{ cm}^{-3}$ and temperatures $\gtrsim 7,000 \text{ K}$ (Nisini 2008; Giannini et al. 2015a; Koo et al. 2016). It is within this cooling region that atomic and singly-ionized species, including forbidden line emission from Fe (i.e., [Fe II]), are collisionally excited. These conditions allow [Fe II] emission to remain strong without being collisionally quenched, making it a reliable tracer of the physical and chemical properties of protostellar jets.

For this study, we focus on the Class I protostar TMC1A (IRAS 04365+2535), a $\sim 0.4 M_\odot$, $\sim 2.7 L_\odot$ source located in the Taurus Molecular Cloud at a distance of 140 pc (Galli et al. 2019) and disk viewed at an inclination of $\sim 54^\circ$, representing an evolutionary stage approximately 10^5 years after the onset of star formation (Kristensen et al. 2012; Harsono et al. 2018). Its nested outflow structure consists of a central collimated atomic [Fe II] jet, a wider-angle H_2 shell observed with JWST (Harsono et al. 2023; Assani et al. 2024), and an even broader CO cavity observed with ALMA (Aso et al. 2015; Bjerkeli et al. 2016; Aso et al. 2021). This outflow is embedded within a dense envelope of gas and dust (Di Francesco et al. 2008), which dominates the extinction along the observer's line of sight. Previous NIR extinction measurements toward TMC1A show that extinction decreases with increasing distance from the protostar, reflecting changes in extinction magnitude (column density) along different sightlines (Assani et al. 2024) also seen in other sources (Erkal et al. 2021; Narang et al. 2023; Delabrosse et al. 2024a; Le Gouellec et al. 2024a).

To compare relative NIR/MIR extinction along the jet as a probe of changes in the dust grain size distribution (i.e., dust growth) within the envelope, we adopt an approach that combines excitation models with multi-wavelength embedded [Fe II]

jet emission line data. We focus on line ratios rather than absolute intensities, as ratios are less sensitive to uncertainties in the emitting surface and source geometry. Emission lines originating from the same upper energy level have traditionally served as robust tools for measuring extinction magnitude, as their intrinsic line ratios depend solely on radiative de-excitation rates, determined by the Einstein A-coefficients, and are independent of physical conditions such as density and temperature (e.g., Nisini 2008; Giannini et al. 2015b). Extending this analysis to include emission lines from different upper energy levels, we leverage excitation models to predict a range of intrinsic line ratios across a broader wavelength span.

This approach enables us to compute extinction curves from observational line emission data, compare them with the existing extinction laws, and identify potential variations in extinction along different lines of sight. Using JWST NIRSpec IFU and MIRI MRS spectroscopy, we aim to characterize the extinction toward the TMC1A protostellar jet and assess how it compares to extinction laws derived from diffuse and dense cloud environments away from protostars. This study provides a spatially resolved probe of dust properties in a protostellar envelope, offering new insights into how dust evolves during early star formation.

The paper is organized as follows. In Section 2, we describe the JWST observations and data reduction procedures, detailing the processing of NIRSpec IFU and MIRI MRS spectra and the calculation of observed [Fe II] emission line intensities along the jet (Section 2.1). This is followed by a description of our excitation model for [Fe II] in Section 3. In Section 4, we outline our method for determining relative extinction between gas emission lines, beginning with extinction differences in the simpler case of lines originating from the same upper energy level in the NIR (Section 4.1). We then extend this analysis to the MIR (Section 4.3), using electron density constraints derived from NIR lines (Section 4.2) as a reference for comparing relative extinction. Finally, we consider cases where NIR and MIR lines trace different excitation conditions and examine how these differences influence the derived MIR extinction curves (Section 4.3). In Section 5, we discuss the interpretations of our results in the context of existing extinction laws and dust grain evolution, and we conclude with a summary of our findings in Section 6.

2. Observations and Data Reduction

We present NIRSpec IFU and MIRI MRS observations of TMC1A. The NIRSpec data, originally introduced in Harsono et al. (2023) (PID: 2104, PI: Harsono), focused on the [Fe II] lines discussed in Assani et al. (2024). The MIRI MRS observations, presented here for the first time, were obtained on March 4, 2023, as part of the JWST Observations of Young ProtoStars (JOYS) Guaranteed Time Observations (GTO) program (PID: 1290, PI: E. van Dishoeck).

The NIRSpec IFU data, obtained on February 12, 2022, were reprocessed using JWST pipeline v1.11.4 (Bushouse et al. 2023), incorporating updated calibration files (JWST_1123.PMAP) (Greenfield & Miller 2016). This version improved cosmic ray artifact handling, including snowball features, and enhanced flux calibration compared to previous reductions (v1.9.6) used in Harsono et al. (2023). Consistent with prior reductions, we skipped the Stage 3 outlier detection step to avoid excessive flagging of saturated pixels and strong emission lines (Sturm et al. 2023). The final spectral cubes were manually inspected, and problematic spaxels were masked after continuum subtraction and applying signal-to-noise thresholds.

The MIRI MRS observations covered a wavelength range of 4.9–28.6 μm with a total integration time of 600 seconds across three sub-bands, each integrated with 36 groups in FASTR1 mode and two dithers optimized for extended emission. The data were processed using JWST pipeline v1.16.1 (Bushouse et al. 2024), with jwst1303.pmap as the calibration reference system. The Detector1Pipeline was applied to the uncal files with default settings to produce detector images, which were subsequently calibrated using the Spec2Pipeline. During this step, the fringe flat was subtracted from the data, residual fringe correction was applied, and a pixel-by-pixel background subtraction was performed using dedicated background detector images. A custom bad-pixel correction was applied using the VIP package (Christiaens et al. 2023). The final data cubes were created using the Spec3Pipeline with the drizzle algorithm (Law et al. 2023), processing each band and channel independently. Due to a telescope mispointing, one of the two dither pointings in channel 1 did not cover the target, so only a single dither was used for that channel, while both dithers were used for all other channels. Background observations were taken immediately prior to the science exposures, using a single dither with 36 groups. The absolute flux calibration uncertainty for the MIRI-MRS observations is estimated to be $5.6\% \pm 0.7\%$ (Argyriou et al. 2023).

To align the datasets, we determined the protostar’s position by fitting a 2D Gaussian function to the point spread function (PSF) in the NIRSpec and MIRI data. The PSF accounts for diffraction effects caused by JWST’s hexagonal mirror structure. For NIRSpec data, the centroid was calculated at wavelengths greater than 4 μm using the G395H grating, while for MIRI data, centroids were derived independently for each spectral channel. These centroids were then used to spatially align the datasets, ensuring accurate correspondence of the protostar’s position across wavelengths. After alignment, the data were interpolated onto a common spatial grid using the 0.1'' pixel scale of the NIRSpec IFU data. This resolution over-samples the native MIRI pixel scale (0.196–0.273''), but facilitates uniform region selection and comparison across wavelengths.

2.1. Observed Line Intensities

This analysis focuses on [Fe II] emission lines relevant to our excitation models (Section 3), building on NIR detections reported in Assani et al. (2024) and 4 new MIR [Fe II] lines. In the NIR, we focus on the "a⁴D" transitions which are detected across the jet and tend to be bright lines ($I_{\lambda}/I_{1.644} > 10^{-2}$). We omit lines that are heavily blended—specifically, the 1.748 μm line (blended with H₂) and the 4.889 μm line (blended with CO v=1-0). The final dataset includes all "a⁴D" transition detections along with the MIRI-detected lines 5.34, 17.99, 24.52 and 25.99 μm . A complete list of these lines, along with their atomic properties, including energy levels, Einstein A-coefficients, and critical densities, is provided in Table A.1.

Observed line intensities were measured at four distinct locations along the blue-shifted axis of the TMC1A jet, focusing on the base of the jet (closer to the protostar) and the intensity peaks previously identified in Assani et al. (2024). These regions are shown as circular, color-coded apertures (diameter 0.7'') overlaid on the moment-0 maps in the top panels of Figure 1. This aperture size exceeds MIRI’s native pixel scale (0.196–0.273'') and approximates instrument’s diffraction limit across the relevant wavelengths ($\sim 0.2''$ at 5 μm , $\sim 0.7''$ at 18 μm , and $\sim 1''$ at 26 μm ; Law et al. 2023), providing consistent spatial sampling across both NIRSpec and MIRI datasets while minimizing undersampling effects at longer wavelengths.

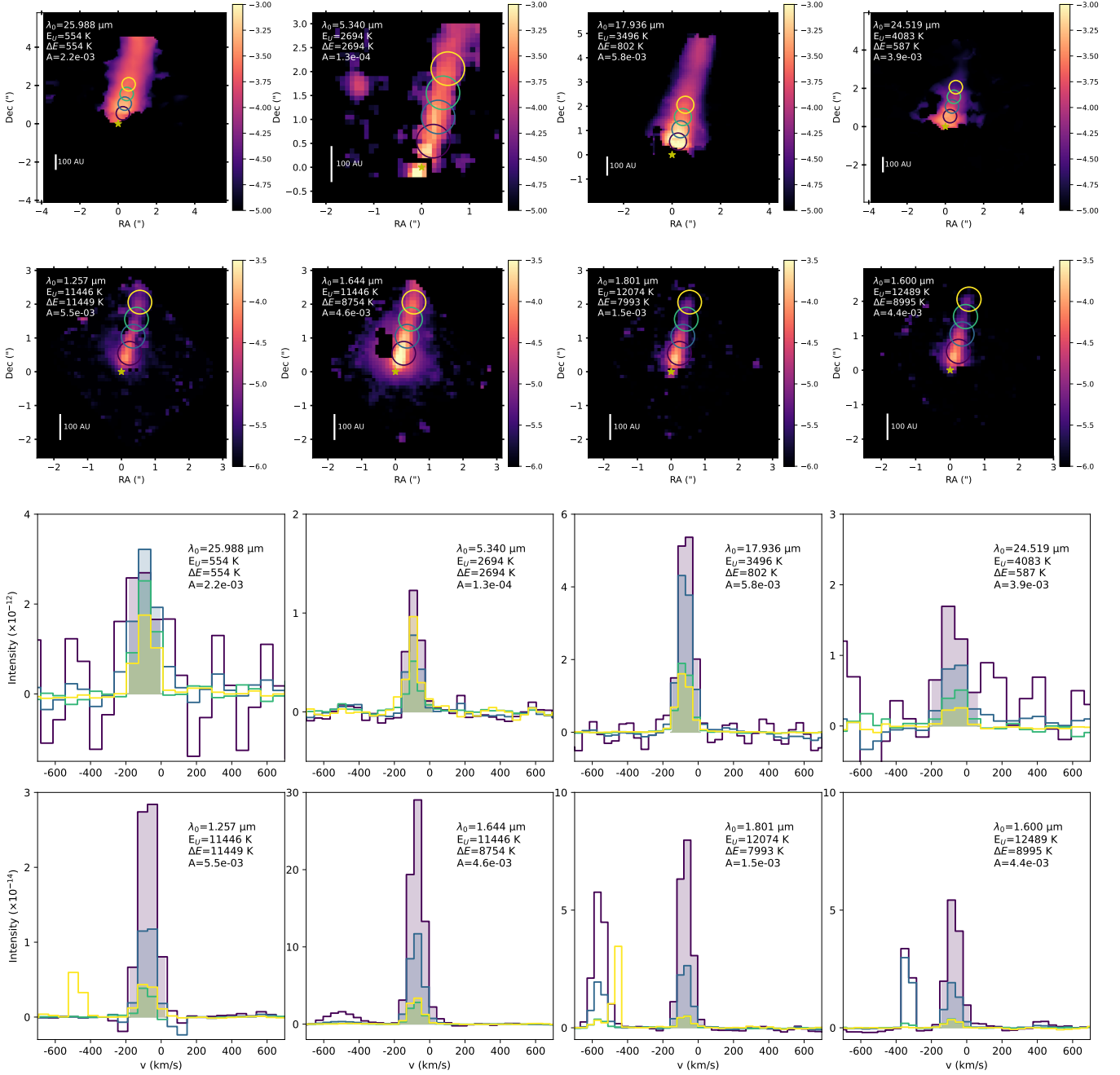


Fig. 1: [Fe II] emission lines used in this study and detected with NIRSpect and MIRI, arranged in order of increasing upper energy (E_U/k). **Top panels:** moment-0 maps (in units of $\text{erg s}^{-1} \text{cm}^{-2} \text{sr}^{-1}$), constructed by integrating the emission across the frequency range indicated by the shaded regions in the corresponding spectra below. Although integration is performed in frequency space, the x-axis is displayed in velocity (km s^{-1}) for clarity. A 3-sigma threshold is applied. The maps are overlaid with circular, color-coded apertures ($0.7''$) used consistently throughout this study. **Bottom panels:** spectra (in units of $\text{erg s}^{-1} \text{cm}^{-2} \text{sr}^{-1} \text{Hz}^{-1}$) extracted from each aperture, with shaded regions highlighting the velocity range used for integration, primarily focusing on blue-shifted emission. Each subplot includes the rest wavelength (λ_0), transition and upper energies (ΔE , E_U), and Einstein-A value for reference.

To extract line intensities, we summed over each aperture at every spectral channel to produce a 1D spectrum for each region (bottom panels of Figure 1). Line intensities (in $\text{erg cm}^{-2} \text{s}^{-1} \text{sr}^{-1}$) were then computed by integrating the continuum-subtracted spectra in frequency space over ~ 3 – 4 channels (corresponding to a velocity range of ~ 150 – 200 km/s), tailored to encompass the full line while maintaining a consistent integration range across apertures for each line (shaded regions in the bottom panels of Figure 1). The resulting intensities and line ratios (relative to the $1.644 \mu\text{m}$ line) are reported in Table A.2.

3. The Iron Line Emission Model

To model the intrinsic line intensities for [Fe II], we use the CLOUDY spectral synthesis code (Ferland et al. 2017; Chatzikos et al. 2023), which simulates physical and chemical processes in the ionized gas. We set up a single-zone calculation—assuming a uniform density and temperature—over a grid of gas densities and temperatures, considering radiative decay and collisional processes such as collisional excitation (where free electrons transfer kinetic energy to bound

electrons, raising them to higher energy states) and collisional de-excitation (where collisions lower excited atoms to lower energy states). We disable photoionization and Ly α pumping in our model to remove contributions from radiative excitation, as their influence on [Fe II] emission in jets remains uncertain. Since our technique for inferring extinction curves involves only ratios of [Fe II] lines, which are controlled by the relative level populations of Fe⁺, which, in turn, depend only on the density of electrons (the primary collider) and electron temperature T_e in K, we follow Verner et al. (1999) and adopt solar abundances (Grevesse et al. 2010) with a fixed, large Fe abundance (Fe/H = 100), a simple technique to leverage the complex machinery of the CLOUDY code to perform relatively straightforward excitation calculations that depend only on n_e and T_e .

For this study, we adopt the Verner et al. (1999) [Fe II] spectroscopic dataset, which includes 371 energy levels and spans transitions from the infrared to the ultraviolet. CLOUDY defaults to the Smyth et al. (2019) dataset, which extends to high temperatures for UV, and was found to best reproduce the observed UV and optical [Fe II] spectra in the case of an AGN (Sarkar et al. 2021). Differences in predicted line ratios between datasets arise from uncertainties in Einstein A-coefficients (~30–50%) and collision strength calculations, which influence the final level populations. We find that Verner et al. (1999) reproduces near- and mid-IR [Fe II] line ratios with electron density and temperature dependencies consistent with previous non-LTE models used for protostellar jets and Herbig-Haro (HH) objects (e.g., Giannini et al. 2015a; Koo et al. 2016). Collisional strengths in the Verner et al. (1999) dataset for all quartet and sextet transitions are taken from Zhang & Pradhan (1995) with transition rates taken from Quinet, P. et al. (1996). The model estimates a [Fe II] line ratio of $I_{1.257}/I_{1.644} = 1.18$, which depends solely on the relative Einstein A-coefficients and transition frequencies, and remains constant across n_e and T_e . This value is consistent with empirically derived intrinsic ratios of 1.11–1.20 (Giannini et al. 2015b), and is commonly used to estimate extinction magnitudes (Assani et al. 2024; Erkal et al. 2021). Therefore, we adopt the Verner et al. (1999) dataset, since a detailed comparison of infrared dataset performance is beyond the scope of this study.

We adopt a model grid with electron densities ($n_e \sim 10^3 - 10^6 \text{ cm}^{-3}$) and temperatures (5,000–20,000 K), based on shock studies indicating that NIR and MIR [Fe II] lines trace low-ionization gas with temperatures above 7,000 K and electron densities $n_e \sim 10^3 - 10^6 \text{ cm}^{-3}$ (e.g., Nisini 2008; Giannini et al. 2015a; Koo et al. 2016).

4. Differential Extinction in NIR and MIR

We compare observed line ratios with intrinsic ratios from the excitation model to determine extinction differences between the NIR and MIR. Extinction modifies the observed ratio as:

$$r_{\text{obs}} = r_{\text{model}}(n_e, T_e) \times 10^{-0.4(A_\lambda - A_{\text{ref}})} \quad (1)$$

where r_{obs} is the observed ratio between a NIR or MIR [Fe II] line and the reference line, which in this study is the bright NIR line at 1.644 μm ; r_{model} the intrinsic line ratio predicted by the excitation model as a function of n_e and T_e ; and A_λ and A_{ref} represent the extinction at the observed and reference wavelengths, respectively. Rearranging, the difference in extinction is given by:

$$\Delta A_\lambda \equiv A_\lambda - A_{\text{ref}} = -2.5 \log_{10} \left(\frac{r_{\text{obs}}}{r_{\text{model}}(n_e, T_e)} \right) \quad (2)$$

Since ΔA_λ depends only on $r_{\text{obs}}/r_{\text{model}}$, it directly quantifies the deviation between observed and intrinsic line emission ratios due to differential extinction relative to the reference wavelength.

To compare the derived extinction differences with commonly used extinction curves, we normalize ΔA_λ by the extinction at the reference wavelength. The normalized extinction ratio is given by

$$\beta_\lambda \equiv \frac{A_\lambda}{A_{\text{ref}}} = \frac{\Delta A_\lambda}{A_{\text{ref}}} + 1 \quad (3)$$

The reference extinction, $A_{1.644}$, is determined for each aperture along the jet using observed [Fe II] integrated line ratios in the near-IR, where commonly used extinction curves show minimal deviation across 1–2 μm (see Sec 1). In this study, we use the bright 1.257/1.644 line pair, which arises from the a⁴D J=7/2 fine-structure state, to calculate $A_{1.644}$ following equation 1 in Assani et al. (2024), using β values ($\beta = A_{1.257}/A_{1.644}$) from established near-IR extinction curves (e.g., Cardelli et al. 1989; Weingartner & Draine 2001; Pontoppidan et al. 2024). The resulting $A_{1.644}$ values for each aperture and extinction curve are listed in Appendix Table A.3. Starting with the aperture closest to the protostar (purple, Fig. 1) and moving outward along the jet axis (yellow), we find $A_{1.644} = 4.11, 4.23, 4.00$, and 3.57 (corresponding to $A_V \sim 20\text{--}17$), with a standard deviation of ~10% between extinction curves and less than 1% variation between $R_V=3.1$ and 5.5 within each curve.

To determine extinction differences between MIR lines and NIR lines (particularly the 1.644 μm line), we begin by establishing a robust reference extinction in the NIR. We first analyze extinction differences of NIR lines that share the same upper energy state as the 1.644 μm line (a⁴D J=7/2), as their intrinsic ratios are independent of physical conditions. This allows us to derive ΔA_λ without uncertainty due to density or temperature effects. Next, we extend our analysis to NIR lines with different upper energy states, which provide a constraint on electron density (n_e). This serves as a key reference for evaluating extinction in the mid-IR, where both n_e and T_e influence the intrinsic line ratios. Finally, we compare NIR and MIR extinction properties and assess how potential differences in the physical conditions (n_e, T_e) among NIR and MIR emitting regions impact the interpretation of relative NIR/MIR extinction.

4.1. NIR Extinction Constraints Using Lines from the Same Upper Energy Level

To begin, we validate our line-based extinction method using NIR [Fe II] lines that share the same upper energy level as the 1.644 μm line (a⁴D J=7/2). These line ratios are insensitive to variations in n_e and T_e , making them ideal for isolating extinction effects. This provides a clean reference for computing ΔA_λ without uncertainty from physical conditions, before extending the analysis to lines with different upper states.

The top panel of Figure 2 presents the observed ('o', not corrected for extinction) and the modeled ('*') line ratios for the a⁴D J=7/2 upper state across all four jet locations (see Figure 1). The middle panel shows the relative extinction differences (ΔA_λ) computed using Equation 2, referenced to the 1.644 μm line. Lines with $\lambda < 1.644 \mu\text{m}$ (e.g., 1.257, 1.321, and 1.327 μm) exhibit positive extinction differences ($\Delta A > 0$), indicating greater extinction compared to the 1.644 μm line. Conversely, the 1.809 μm line has a negative extinction difference ($\Delta A < 0$), implying lower extinction. This confirms that the extinction curve in the 1–2 μm range has a negative slope, where shorter wavelengths

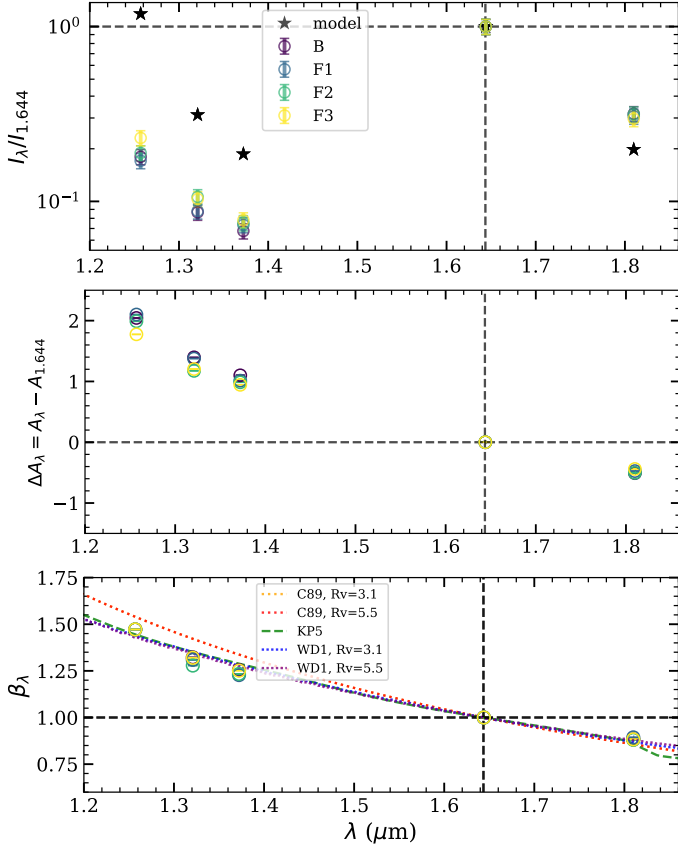


Fig. 2: Near-infrared (NIR) extinction of $a^4\text{D } J=7/2$ lines relative to the $1.644 \mu\text{m}$ line (horizontal and vertical dashed lines.). **Top:** Observed ('o') and modeled ('*') line ratios for all four jet locations in this study. **Middle:** The difference in extinction relative to the $1.644 \mu\text{m}$ line. **Bottom:** Derived β_λ values, normalized by the extinction at $1.644 \mu\text{m}$, which is computed as an average over existing NIR extinction curves—C89 Cardelli et al. (1989), and modeled extinction curves—WD1 Weingartner & Draine (2001), KP5 Pontoppidan et al. (2024). We include $R_V = 3.1$ and $R_V = 5.5$ for applicable curves to illustrate that NIR extinction in the $1.2\text{--}1.8 \mu\text{m}$ range is largely independent of R_V and shows minimal differences between independent studies. Dashed lines mark the reference line ratio, extinction difference, and β_λ value at $1.644 \mu\text{m}$ (horizontal) and the wavelength of $1.644 \mu\text{m}$ (vertical) in all three panels.

suffer more extinction than longer wavelengths, consistent with previous near-IR extinction studies (e.g., Cardelli et al. 1989; Mathis 1990; Gordon et al. 2023). Additionally, the extinction differences exhibit spatial dependence across jet locations, with sightlines closer to the protostar ('B'/purple, 'F1'/blue) showing larger ΔA values at $\lambda < 1.644 \mu\text{m}$. This pattern aligns with the finding that total extinction magnitude decreases with distance from the protostar along sightlines toward the TMC1A jet, as demonstrated in Assani et al. (2024). Consequently, normalizing by the total extinction at each jet location should account for these differences, revealing a more intrinsic extinction trend across locations.

The negative slope observed in our derived ΔA_λ values (middle panel) and the close agreement between our derived β_λ values and independent extinction curves and models (bottom panel) confirm the consistency of the extinction curves in the $1.2\text{--}1.8$

μm range. This consistency reinforces the reliability of using a gas line in this range—such as $1.644 \mu\text{m}$ —as a reference for measuring relative extinction differences. Moreover, having established a well-constrained extinction correction in the NIR, we can now use these NIR lines to probe the physical conditions of the gas emitting these lines, specifically placing constraints on the electron density (n_e).

4.2. Electron Density Constraints from NIR Lines

We now extend our analysis to all observed $a^4\text{D}$ transitions in the near-IR to constrain the electron density (n_e) at each jet location (see Figure 1). The line ratios of $a^4\text{D}$ transitions, which originate from states with similar but slightly different upper-level energies ($E_{\text{upper}} = 11,446\text{--}12,729\text{ K}$) and distinct critical densities ($n_{\text{crit}} \approx 4\text{--}7 \times 10^4 \text{ cm}^{-3}$ at $T = 10,000\text{ K}$), are relatively insensitive to temperature but remain sensitive to electron densities in the $10^3\text{--}5 \text{ cm}^{-3}$ range. This makes them well suited for quantifying n_e in the near-IR, where extinction curves are well established.

The derived electron density is not only important in its own right (as a key physical quantity of the NIR line emitting gas in the jet), but it also serves as a starting point for discussing the electron density in the MIR line emitting region, which is unknown without a firm knowledge of the extinction law for the protostellar envelope where the jet is embedded and may or may not be the same as that in the NIR line emitting gas. This distinction is particularly relevant as the MIR lines arise from lower excitation levels and may trace gas under different physical conditions (see Section 4.3 below).

Figure 3 presents three examples NIR [Fe II] $a^4\text{D}$ line ratios used to determine electron density. The predicted line ratios from the [Fe II] model are plotted as a function of electron density across temperatures from $5,000$ to $20,000\text{ K}$. Observed ratios (circles) and extinction-corrected ratios (squares) are shown with uncertainties. We adopt a constant $\sim 15\%$ uncertainty in extinction for simplicity, consistent with the typical deviations between near-IR extinction curves (see Table A.3) and uncertainties in the Einstein A-values (Giannini et al. 2015b), which result in larger uncertainties for the corrected ratios than for the observed ones. Electron density uncertainties primarily arise from (1) uncertainty in the intrinsic line ratios, broadening the possible n_e range by approximately a factor of two, and (2) temperature-dependent differences in electron density for a given ratio, which are typically small ($< 5\%$).

Near the protostar, electron density estimates approach the critical density (n_{crit}) of these transitions. Since line ratios become insensitive to the density at $n_e \gtrsim n_{\text{crit}}$ due to thermalization effects (as the gas approaches LTE conditions), constraining electron densities in such regions becomes increasingly uncertain. As a result, the density estimates in the bright region ('B'/purple) should be interpreted as lower limits. Further from the protostar, intensity ratios relative to the $1.644 \mu\text{m}$ line are lower, leading to consistently lower and well-constrained electron density estimates.

Across 13 NIR $a^4\text{D}$ line ratios, electron density estimates remain internally consistent, with differences limited to a factor of ~ 2 at each jet location (see Table A.4). The results show a clear trend of decreasing electron density along the jet axis: $\bar{n}_e = (3.6 \pm 1.0) \times 10^4 \text{ cm}^{-3}$ (knot "B"/purple), $(2.4 \pm 0.6) \times 10^4 \text{ cm}^{-3}$ ("F1"/blue), $(1.5 \pm 0.5) \times 10^4 \text{ cm}^{-3}$ ("F2"/green), and $(8.0 \pm 3.0) \times 10^3 \text{ cm}^{-3}$ ("F3"/yellow). While uncertainties in adjacent regions overlap in some cases, the overall trend of decreasing electron density with distance from the protostar remains ro-

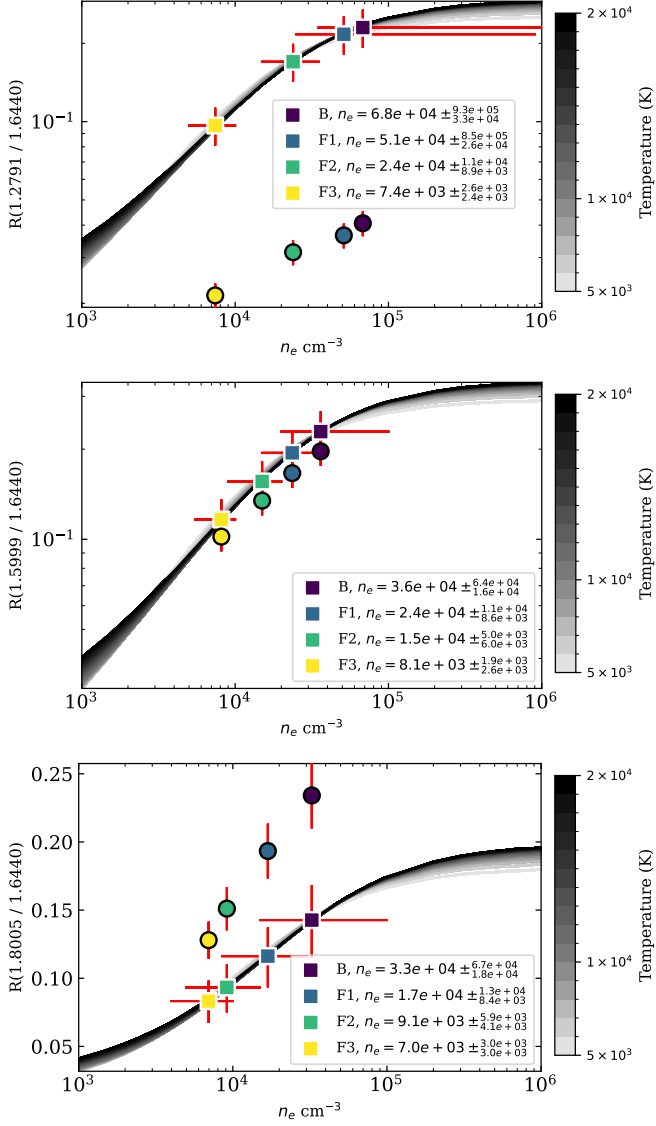


Fig. 3: Examples of density-sensitive NIR line ratios, where the CLOUDY model predictions are shown as solid lines shaded by temperature. Observed line ratios with uncertainties are represented by circles, while extinction-corrected ratios are shown as squares color-coded by jet location (see Fig. 1). The extinction-corrected ratio, accounting for uncertainties, determines the electron density from the model, aligning with the x-axis position of both observed and corrected ratios. **Top:** A shorter-wavelength line is more affected by extinction, leading to an increased ratio after correction. **Middle:** A line ratio with similar rest wavelengths, minimally affected by extinction, where the observed ratio closely matches the expected electron density. **Bottom:** A longer-wavelength line less affected by extinction, causing the ratio to decrease after correction. Following extinction correction using established NIR curves (Section 4.1), all corrected ratios fall within the model-predicted range, showing consistent electron density trends across jet locations and line pairings. This electron density serves as a starting point for comparing relative extinction in the NIR/MIR (Section 4.3).

bust. The electron density drops between the bright region (B) and the third peak (F3) exceeds observational uncertainties in most ratios, further reinforcing this trend.

Now that the electron density has been determined using NIR [Fe II] gas lines at each jet location, we can use these values as reference points to assess relative extinction between the NIR and MIR along each line of sight toward the TMC1A jet.

4.3. Relative Extinction between NIR and MIR

To determine the relative extinction between the NIR and MIR, we compare observed [Fe II] line ratios of MIR transitions (a⁶D, a⁴F at 5.3, 17.0, 24.5, and 26 μm) relative to the 1.644 μm line with intrinsic model ratios. We first assume that the NIR and MIR lines along the same sightlines originate from the same physical region, implying identical excitation conditions governed by the same n_e and T . Next, we explore the case where MIR lines along the same sightlines trace gas with conditions different from NIR lines, with different values of n_e and/or T .

The electron density derived from NIR lines (Sect. 4.2) serves as the reference for these comparisons at each jet location. Uncertainties in electron density and temperature contribute to the overall uncertainty range. We adopt a standard reference temperature of 10,000 K, consistent with shock models, where NIR and MIR lines become emissive at temperatures $\geq 7,000$ K (Nisini 2008; Giannini et al. 2015a; Koo et al. 2016). To account for uncertainties, we use a lower bound of 5,000 K.

4.3.1. Case 1: Same Physical Conditions

In the scenario where the NIR and MIR [Fe II] emission lines along the same sightlines originate from the same physical region, we first calculate the modeled line ratios assuming the same electron density and temperature for both MIR and NIR lines, including the reference line at 1.644 μm .

Figure 4 shows the derived extinction for each line of sight toward the TMC1A jet. The left panels show NIR-derived extinction in the 1.2–1.85 μm range, including additional a⁴D lines not used to derive the electron density, which follows the trend observed in Sect. 4.1. The right panels show extinction derived from the four MIR lines observed with MIRI.

The observed MIR line fluxes are comparable to or higher than that of the 1.644 μm line (with ratios $r_{\text{obs}} \sim 1$ –10), which is very different from the intrinsic line ratios modeled, which are below unity (with $r_{\text{model}} < 1$). The difference is caused by the fact that the reference NIR line at 1.644 μm experiences stronger extinction than the MIR lines, which is reflected by the negative ΔA_λ shown in the middle right panel of Fig. 4.

Extinction at each jet location follows a pattern where bright regions (B, F1) exhibit higher MIR extinction than regions farther from the protostar (F2, F3), consistent with increased column density closer in. Our inferred extinction at 5.34 μm is low ($\beta_\lambda \sim 0$), likely setting a lower limit since it is comparable to or less than the least extinct curve at that wavelength (WD1, $R_V = 3.1$). In contrast, extinction at 17.93, 24.52, and 25.99 μm is usually higher than the comparison curves, indicating greater attenuation at these wavelengths compared to that expected from the comparison curves.

Since $r_{\text{obs}} > r_{\text{model}}$ for the MIR lines, we find $\Delta A_\lambda < 0$, and any additional suppression of the observed MIR intensity due to line blending would only make ΔA_λ less negative, thereby increasing β_λ . This could be the case for the [Fe II] 17.936 μm line, which is spectrally close to the H₂ $v = 1$ –1 S(1) line at 17.94 μm . However, as a first-order approximation, we built an H₂ excitation model and interpolated the column density of H₂ molecules in the upper state ($v_u = 1$, $J_u = 3$) based on the energy of the corresponding upper state of H₂ 1–1 S(1). We then estimated the H₂ 1–1 S(1) line flux using the Einstein coefficient of spontaneous

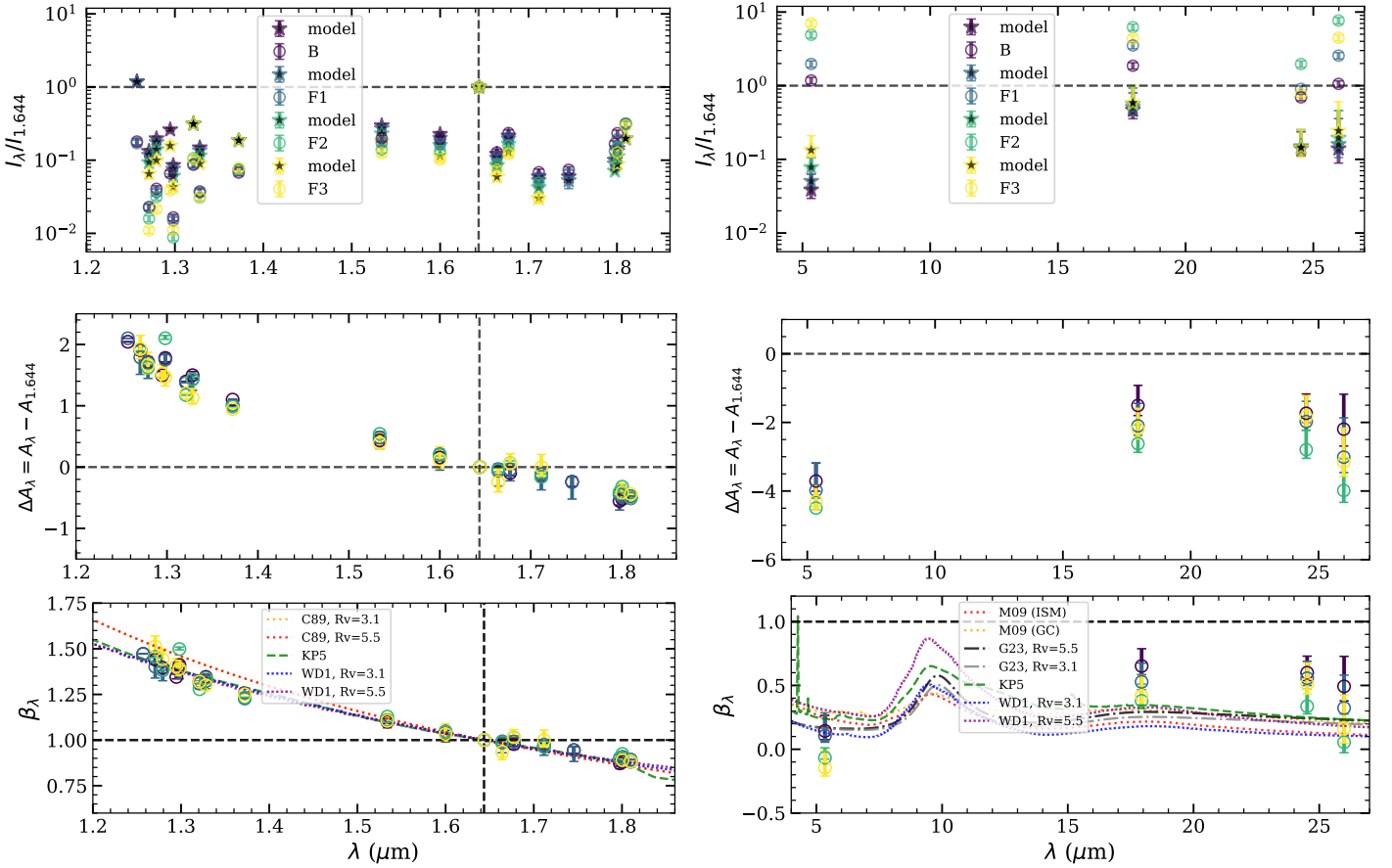


Fig. 4: NIR and MIR extinction toward the TMC1A jet. Same as Figure 2, but extended to include additional a⁴D lines in the NIR (left) used for n_e derivation, along with MIR lines (right). Model scatter points correspond to the derived electron density at 10,000 K (see Sect. 4.2), with uncertainties reflecting the uncertainty range in the determined n_e value and temperatures from 5,000–10,000 K. Commonly used NIR/MIR extinction curves are overplotted for comparison (see text).

emission, assuming an extinction law (KP5; Pontoppidan et al. (2024)) and corresponding extinction value. This allowed us to calculate the fraction of the observed 17.936 μm line that originates from H₂ and [Fe II]. We find the H₂ contribution is $\ll 1\%$, confirming that [Fe II] dominates at this wavelength.

4.3.2. Case 2: Diverging Physical Conditions between NIR and MIR lines

The observed [Fe II] lines may originate from gas with different excitation conditions. This posits that the emitting regions are stratified, where higher-excitation lines (e.g., those in the NIR) predominantly trace hotter and/or denser gas, while lower-excitation lines (e.g., those in the MIR) arise from cooler and/or less dense regions along the same line of sight (within the effective telescope beam).

To explore this possibility, we consider a simplified scenario in which the NIR ($\lambda < 5 \mu\text{m}$) and MIR ($\lambda > 5 \mu\text{m}$) lines trace two distinct temperature and density components, with

$$r_{\text{model}} = \frac{I_{\lambda_{\text{MIR}}}(f_{n_e} n_e, f_T T_e)}{I_{1.644}(n_e, T_e)} \quad (4)$$

where f_{n_e} and f_T represent the fractional electron density and temperature of the MIR-emitting gas relative to those inferred from the NIR a⁴D line ratios (see Sect. 4.2).

For temperatures above 5,000 K, predicted line ratios converge at a given electron density, resulting in minimal temperature dependence on the derived β_λ values. This is seen in the top subplot of Fig. 5, where the MIR lines are assumed to originate from gas at half the temperature of the NIR lines ($f_T = 0.5$, $T_{\text{MIR}} = 5,000 \text{ K}$, $T_{\text{NIR}} = 10,000 \text{ K}$). The derived MIR β_λ values are almost indistinguishable from the reference case of $f_T = 1$ and $f_{n_e} = 1$ shown in the lower-right panel of Fig. 4.

In contrast, electron density has a more pronounced effect on β_λ . The middle subplot ($f_T = 1.0$, $f_{n_e} = 0.5$) shows that lowering the electron density systematically reduces β_λ , consistent with an increased MIR/NIR line ratio that decreases the relative difference between observed and modeled values. The bottom subplot ($f_T = 0.5$, $f_{n_e} = 0.5$) shows a similar β_λ profile to the middle case, reinforcing that the electron density difference has a stronger influence on the derived extinction than temperature differences.

5. Discussion

We developed a new technique for determining the MIR extinction in the protostellar envelope using JWST IFU observations of several [Fe II] NIR and MIR emission lines, leveraging the well-determined NIR extinction curve and excitation model for line ratios. It is applied to the atomic jet toward Class I protostar TMC1A which is embedded in a large scale infalling en-

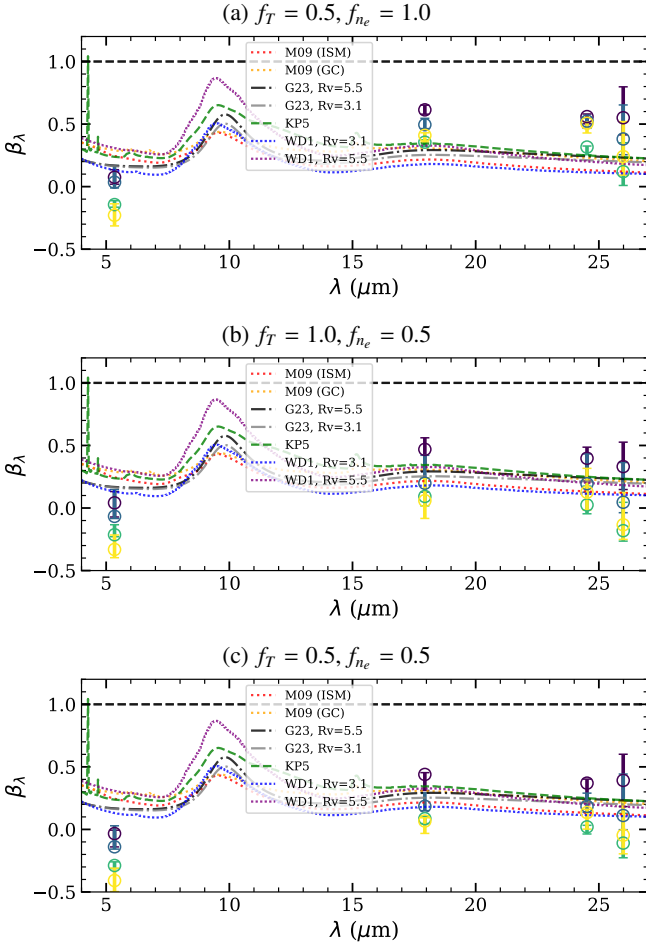


Fig. 5: Derived MIR extinction from [Fe II] lines ($\lambda > 5 \mu\text{m}$) tracing different excitation conditions compared to NIR [Fe II] lines. The plots show MIR extinction, where MIR [Fe II] lines trace different excitation conditions (n_e , T_e) than NIR [Fe II] lines. **Top** β_λ values assuming MIR line intensities correspond to gas at half the NIR-traced temperature ($f_T = 0.5$) with the same electron density ($f_{n_e} = 1$). **Middle** Same temperature as NIR-traced gas ($f_T = 1.0$), but assuming MIR lines trace half the electron density ($f_{n_e} = 0.5$). **Bottom** Both temperature and electron density are halved ($f_T = 0.5$, $f_{n_e} = 0.5$).

velope. This technique provides a spatially resolved constraint on extinction along different sightlines to the jet, offering an independent measurement distinct from background star methods applied to diffuse and dense clouds away from protostars (e.g., McClure 2009); it complements opacity measurements of volatile ice features in protostellar envelopes along similar sightlines. (e.g., Tyagi et al. 2024). Figure 6 illustrates this distinction, with the top panel showing extinction measured from background stars and the bottom panel representing embedded jet sightlines that pass through a large and dense, infalling envelope.

If the MIR lines originate from gas in the embedded jet with physical conditions (electron density n_e and temperature T) similar to those of the NIR line emitting region along the same sightlines, we find systematically higher MIR extinction through the protostellar envelope compared to the empirical high-extinction regime derived by McClure (2009). It also exceeds the $R_V=5.5$ case from Weingartner & Draine (2001) and the KP5 model from Pontoppidan et al. (2024) (see the lower-

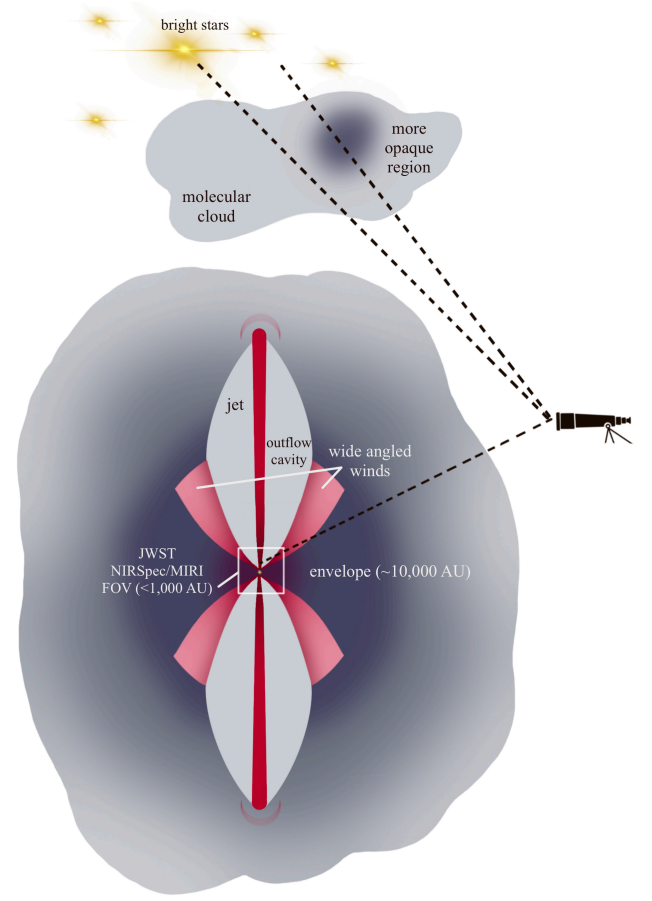


Fig. 6: Schematic illustrating extinction geometry in two contexts: (top) background star extinction studies, and (bottom) protostellar envelopes. The bottom panel (adapted from Fig. 5 of van Dishoeck et al. (2011)) shows a forming star embedded in a large infalling envelope, with bipolar jets carving outflow cavities. The JWST NIRSpec/MIRI field of view probes <1000 AU scales, with dashed lines tracing the line-of-sight path through the dense envelope, where most extinction occurs. In contrast, the top panel illustrates background stars viewed through diffuse and dense regions of a molecular cloud (e.g. McClure 2009), probing more pristine dust that has not yet experienced collapse or been processed by star formation. While the top probes molecular cloud dust, the embedded jet sightlines (bottom) trace extinction through evolved, denser material. Higher MIR extinction near the protostar—if MIR and NIR lines trace similar gas—may indicate a change in the grain size distribution potentially due to further grain growth as the cloud condenses and collapses to form the central protostar.

right panel of Fig. 4). These models describe dust populations with larger maximum grain sizes than those in the diffuse ISM. The alignment of McClure (2009) with the $R_V=5.5$ case has been interpreted as evidence for dust grain growth in denser cloud regions. If the MIR and NIR emission lines trace the same excitation conditions, the higher inferred extinction in the MIR toward the embedded jet suggests differences in the grain size distribution such as the presence of even larger dust grains along these sightlines. This result adds weight to the conclusion of Valdivia et al. (2019) and Le Gouellec et al. (2020) that dust grains must have grown significantly in protostellar envelopes—since relatively long-wavelength local IR photons can only spin them up

efficiently through radiative torques if the grains are sufficiently large, enabling magnetic alignment and the observed levels of dust polarization.

If the MIR emission lines trace lower electron density and temperature than the NIR lines, then the modeled intrinsic MIR lines would be weaker, yielding a lower inferred MIR extinction, with the resulting β_λ values falling within the range predicted by background star studies (see Sec 4.3.2). In this case, the extinction curve does not indicate significant changes in grain size distributions such as dust growth beyond what is inferred along high-extinction sightlines of dense clouds. This result is still highly significant because it implies that, even along the same sightlines to the embedded jet, the MIR lines must originate from gas with properties different from those of the NIR line emitting gas. This could happen if, e.g., the MIR and NIR lines trace different regions behind spatially unresolved shocks in the telescope beam. Differences in excitation conditions between NIR and MIR lines have been observed in the case of H₂ outflows (e.g., Vleugels et al. 2025), but to our knowledge, this has not yet been demonstrated for atomic lines from the same ionization state. Our result highlights the important point that it would be difficult to accurately infer the physical properties of the MIR line-emitting gas in the embedded jet unless the MIR extinction curve in the foreground protostellar envelope is well characterized independently.

The method described in this paper, leveraging wide spectral coverage and integral field unit (IFU) observations, could be extended to other embedded astrophysical environments. Atomic and molecular tracers, such as forbidden lines, hydrogen recombination lines, H₂ with their wide spectral coverage across infrared and radio wavelengths, offer promising opportunities for applying this technique. If these tracers originate from the same spatial region and their line intensities or ratios can be reliably modeled, extinction curves could be determined. Additionally, applying this method to species tracing spatially distinct regions (e.g., spatially nested outflows) and comparing them self-consistently within the same source could provide deeper insights into the dust properties across these regions, offering a unique perspective on the role of dynamic processes in star formation (particularly outflows) in shaping dust. Expanding this approach to more sources at different stages of star formation and along diverse lines of sight would enhance our understanding of dust evolution within protostellar environments and throughout star formation.

6. Conclusions

This study investigates the extinction properties and evidence of dust processing in the protostellar envelope surrounding the embedded [Fe II] jet of the Class I protostar TMC1A using JWST NIRSpec and MIRI observations and a novel technique. By combining high-sensitivity, multi-wavelength emission line data with excitation models, we derived localized extinction curves along sightlines to the embedded jet and compared them to extinction laws derived from dark cloud populations. These efforts aimed to understand how star formation processes influence the surrounding dust populations, contributing to differences in line-of-sight extinction. We summarize our findings as follows:

1. We have developed a new method for characterizing the NIR-MIR extinction of the material in the protostellar envelope along the lines of sight to an embedded [FeII] jet based on JWST NIRSpec and MIRI observations of line emissions and excitation model predictions of intrinsic line ratios.

2. The modeled intrinsic line ratios depend on electron density and temperature. The electron density can be reasonably well constrained by NIR [Fe II] lines (for which extinction curves are already well characterized), with values ranging from approximately 5×10^3 to 5×10^4 cm⁻³, decreasing farther from the protostar, consistent with prior studies of protostellar outflows.
3. If the MIR lines originate from gas in the embedded jet with electron density n_e and temperature T similar to those of the NIR line emitting region along the same sightlines, we find a systematically higher MIR extinction through the protostellar envelope than those derived by McClure (2009) for dark clouds, the R_V=5.5 case modeled by Weingartner & Draine (2001), and the KP5 model from Pontoppidan et al. (2024). This result adds weight to growing evidence—for example from dust polarization—for significant grain growth in protostellar envelopes.
4. If the MIR emission lines trace lower electron density and temperature than the NIR lines, the inferred MIR extinction falls within the range of the existing values for dark clouds. In this case, there is no direct evidence for a change in the dust size distribution (i.e. grain growth) in protostellar envelopes beyond that in dense dark clouds. Instead, the observed MIR/NIR line ratios and excitation modeling suggest that the MIR and NIR lines originate from different regions along the same sightline within the embedded jet, each characterized by distinct physical conditions.

Acknowledgements. This work was supported in part by an ALMA SOS award, STScI grant JWST-GO-02104.002-A, NSF grant AST-2307199, NASA ATP grant 80NSSC20K0533, and the Virginia Institute of Theoretical Astronomy. This work is based on observations made with the NASA/ESA/CSA James Webb Space Telescope. The data were obtained from the Mikulski Archive for Space Telescopes at the Space Telescope Science Institute, which is operated by the Association of Universities for Research in Astronomy, Inc., under NASA contract NAS 5-03127 for JWST. These observations are associated with GO program #2104. D.H. is supported by a Center for Informatics and Computation in Astronomy (CICA) grant and grant number 110J035319 from the Ministry of Education of Taiwan. D.H. also acknowledges support from the National Science and Technology Council, Taiwan (Grant NSTC111-2112-M-007-014-MY3, NSTC113-2639-M-A49-002-ASP, and NSTC113-2112-M-007-027). A.C.G. acknowledges support from PRIN-MUR 2022 20228JPA3A “The path to star and planet formation in the JWST era (PATH)” funded by NextGeneration EU and by INAF-GoG 2022 “NIR-dark Accretion Outbursts in Massive Young stellar objects (NAOMY)” and Large Grant INAF 2022 “YSOs Outflows, Disks and Accretion: towards a global framework for the evolution of planet forming systems (YODA)”. D.R. acknowledges support by the European Research Council advanced grant H2020-ER-2016-ADG-743029. We also thank Sophia Spiegel for contributing to the schematic shown in Figure 6, which enhances the clarity and impact of this work.

References

- Argyriou, I., Glasse, A., Law, D. R., et al. 2023, *A&A*, 675, A111
Aso, Y., Kwon, W., Hirano, N., et al. 2021, *ApJ*, 920, 71
Aso, Y., Ohashi, N., Saigo, K., et al. 2015, *ApJ*, 812, 27
Assani, K. D., Harsono, D., Ramsey, J. P., et al. 2024, *A&A*, 688, A26
Bjerkeli, P., van der Wiel, M. H. D., Harsono, D., Ramsey, J. P., & Jørgensen, J. K. 2016, *Nature*, 540, 406
Boogert, A. C. A., Gerakines, P. A., & Whittet, D. C. B. 2015, *ARA&A*, 53, 541
Brügger, N., Burn, R., Coleman, G. A. L., Alibert, Y., & Benz, W. 2020, *A&A*, 640, A21
Bushouse, H., Eisenhamer, J., Dencheva, N., et al. 2023, *JWST Calibration Pipeline*
Bushouse, H., Eisenhamer, J., Dencheva, N., et al. 2024, *JWST Calibration Pipeline*
Cacciapuoti, L., Macias, E., Gupta, A., et al. 2024, *A&A*, 682, A61
Caratti o Garatti, A., Ray, T. P., Kavanagh, P. J., et al. 2024, *A&A*, 691, A134
Cardelli, J. A., Clayton, G. C., & Mathis, J. S. 1989, *Astrophysical Journal*, Part 1 (ISSN 0004-637X), vol. 345, Oct. 1, 1989, p. 245-256., 345, 245

- Chatzikos, M., Bianchi, S., Camilloni, F., et al. 2023, *Rev. Mexicana Astron. Astrofis.*, 59, 327
- Christiaens, V., Gonzalez, C., Farkas, R., et al. 2023, *The Journal of Open Source Software*, 8, 4774
- Crapsi, A., van Dishoeck, E. F., Hogerheijde, M. R., Pontoppidan, K. M., & Dullemond, C. P. 2008, *A&A*, 486, 245
- Dartois, E., Noble, J. A., Caselli, P., et al. 2024, *Nature Astronomy*, 8, 359
- Decleir, M., Gordon, K. D., Misselt, K. A., et al. 2025, *The Astronomical Journal*, 169, 99
- Delabrosse, V., Dougados, C., Cabrit, S., et al. 2024a, *arXiv e-prints*, arXiv:2403.19400
- Delabrosse, V., Dougados, C., Cabrit, S., et al. 2024b, *A&A*, 688, A173
- Di Francesco, J., Johnstone, D., Kirk, H., MacKenzie, T., & Ledwosinska, E. 2008, *ApJS*, 175, 277
- Drażkowska, J., Bitsch, B., Lambrechts, M., et al. 2023, in *Astronomical Society of the Pacific Conference Series*, Vol. 534, *Protostars and Planets VII*, ed. S. Inutsuka, Y. Aikawa, T. Muto, K. Tomida, & M. Tamura, 717
- Erkal, J., Nisini, B., Coffey, D., et al. 2021, *ApJ*, 919, 23
- Ferland, G., Chatzikos, M., Guzmán, F., et al. 2017, *Revista mexicana de astronomía y astrofísica*, 53
- Frank, A., Ray, T. P., Cabrit, S., et al. 2014, *Protostars and Planets VI*, 451
- Galametz, M., Maury, A. J., Valdivia, V., et al. 2019, *A&A*, 632, A5
- Galli, P., Loinard, L., Bouy, H., et al. 2019, *Astronomy & Astrophysics*, 630, A137
- Giannini, T., Antonucci, S., Nisini, B., Bacciotti, F., & Podio, L. 2015a, *ApJ*, 814, 52
- Giannini, T., Antonucci, S., Nisini, B., et al. 2015b, *ApJ*, 798, 33
- Gordon, K. D., Clayton, G. C., Decleir, M., et al. 2023, *ApJ*, 950, 86
- Greenfield, P. & Miller, T. 2016, *Astronomy and Computing*, 16, 41
- Grevesse, N., Asplund, M., Sauval, A. J., & Scott, P. 2010, *Ap&SS*, 328, 179
- Harsono, D., Bjerkeli, P., Ramsey, J. P., et al. 2023, *ApJ*, 951, L32
- Harsono, D., Bjerkeli, P., van der Wiel, M. H. D., et al. 2018, *Nature Astronomy*, 2, 646
- Hollenbach, D. & McKee, C. F. 1989, *Astrophysical Journal*, Part 1 (ISSN 0004-637X), vol. 342, July 1, 1989, p. 306-336., 342, 306
- Johansen, A., Blum, J., Tanaka, H., et al. 2014, in *Protostars and Planets VI*, ed. H. Beuther, R. S. Klessen, C. P. Dullemond, & T. Henning, 547–570
- Johansen, A., Ronnet, T., Bizzarro, M., et al. 2021, *Science Advances*, 7, eabc0444
- Koo, B.-C., Raymond, J. C., & Kim, H.-J. 2016, *Journal of Korean Astronomical Society*, 49, 109
- Kristensen, L. E., van Dishoeck, E. F., Bergin, E. A., et al. 2012, *A&A*, 542, A8
- Law, D. R., Morrison, J. E., Argyriou, I., et al. 2023, *The Astronomical Journal*, 166, 45
- Le Gouellec, V. J. M., Greene, T. P., Hillenbrand, L. A., & Yates, Z. 2024a, *ApJ*, 966, 91
- Le Gouellec, V. J. M., Hull, C. L. H., Maury, A. J., et al. 2019, *ApJ*, 885, 106
- Le Gouellec, V. J. M., Lew, B. W. P., Greene, T. P., et al. 2024b, *arXiv e-prints*, arXiv:2410.11095
- Le Gouellec, V. J. M., Maury, A. J., Guillet, V., et al. 2020, *A&A*, 644, A11
- Mathis, J. S. 1990, *ARA&A*, 28, 37
- McClure, M. 2009, *ApJ*, 693, L81
- McClure, M. K., Rocha, W. R. M., Pontoppidan, K. M., et al. 2023, *Nature Astronomy*, 7, 431
- Miotello, A., Testi, L., Lodato, G., et al. 2014, *A&A*, 567, A32
- Narang, M., P., M., Tyagi, H., et al. 2023, *Investigating Protostellar Accretion across the mass spectrum with the JWST: discovery of a collimated jet from the low luminosity protostar IRAS 16253-2429 in a quiescent accretion phase*
- Nisini, B. 2008, in *Jets from Young Stars II*, ed. F. Bacciotti, L. Testi, & E. Whelan, Vol. 742, 79
- Pascucci, I., Beck, T. L., Cabrit, S., et al. 2024, *Nature Astronomy* [arXiv:2410.18033]
- Pontoppidan, K. M., Evans, N., Bergner, J., & Yang, Y.-L. 2024, *Research Notes of the American Astronomical Society*, 8, 68
- Quinet, P., Le Dourneuf, M., & Zeppen, C. J. 1996, *Astron. Astrophys. Suppl. Ser.*, 120, 361
- Sarkar, A., Ferland, G., Chatzikos, M., et al. 2021, *The Astrophysical Journal*, 907, 12
- Smyth, R., Ramsbottom, C., Keenan, F., Ferland, G., & Ballance, C. 2019, *Monthly Notices of the Royal Astronomical Society*, 483, 654
- Sturm, J. A., McClure, M. K., Beck, T. L., et al. 2023, *A&A*, 679, A138
- Tyagi, H., Manoj, P., Narang, M., et al. 2024, *arXiv e-prints*, arXiv:2410.06697
- Tychoniec, Ł., van Gelder, M. L., van Dishoeck, E. F., et al. 2024, *A&A*, 687, A36
- Valdivia, V., Maury, A., Brauer, R., et al. 2019, *MNRAS*, 488, 4897
- van Dishoeck, E. F., Kristensen, L. E., Benz, A. O., et al. 2011, *PASP*, 123, 138
- Verner, E., Verner, D., Korista, K., et al. 1999, *The Astrophysical Journal Supplement Series*, 120, 101
- Vleugels, C., McClure, M., Sturm, A., & Vlasblom, M. 2025, *A&A*, 695, A145
- Weingartner, J. C. & Draine, B. T. 2001, *ApJ*, 548, 296
- Zhang, H. L. & Pradhan, A. K. 1995, *A&A*, 293, 953

Appendix A: Supplemental Material

This appendix contains supplemental tables referenced throughout the main text. Table A.1 lists atomic properties and critical densities for the [Fe II] transitions analyzed in this study. Table A.2 provides the observed continuum-subtracted line intensities and ratios for each jet location. Table A.3 summarizes the extinction values ($A_{1.644}$ and A_V) derived from various extinction curves. Table A.4 presents the inferred electron densities based on corrected line ratios.

λ (μm)	Term _k	J_k	g_k	Energy _k /k (K)	Term _i	J_i	g_i	Energy _i /k (K)	T_{ex} (K)	A_{ki} (s ⁻¹)	n_{crit} (cm ⁻³)
25.988	a6D	7/2	8	554	a6D	9/2	10	0	554	2.05e-03	2.77e+04
5.340	a4F	9/2	10	2694	a6D	9/2	10	0	2694	5.35e-05	1.33e+03
17.936	a4F	7/2	8	3496	a4F	9/2	10	2694	802	6.01e-03	3.46e+04
24.519	a4F	5/2	6	4083	a4F	7/2	8	3496	587	4.17e-03	2.22e+04
1.257	a4D	7/2	8	11446	a6D	9/2	10	0	11446	5.18e-03	6.05e+04
1.321	a4D	7/2	8	11446	a6D	7/2	8	554	10892	1.44e-03	6.05e+04
1.372	a4D	7/2	8	11446	a6D	5/2	6	961	10485	8.93e-04	6.05e+04
1.644	a4D	7/2	8	11446	a4F	9/2	10	2694	8752	5.73e-03	6.05e+04
1.810	a4D	7/2	8	11446	a4F	7/2	8	3496	7950	1.25e-03	6.05e+04
1.249	a4D	5/2	6	12074	a6D	7/2	8	554	11520	4.62e-04	5.11e+04
1.295	a4D	5/2	6	12074	a6D	5/2	6	961	11113	2.23e-03	5.11e+04
1.328	a4D	5/2	6	12074	a6D	3/2	4	1241	10833	1.30e-03	5.11e+04
1.534	a4D	5/2	6	12074	a4F	9/2	10	2694	9380	3.00e-03	5.11e+04
1.677	a4D	5/2	6	12074	a4F	7/2	8	3496	8578	2.38e-03	5.11e+04
1.801	a4D	5/2	6	12074	a4F	5/2	6	4083	7991	1.72e-03	5.11e+04
1.279	a4D	3/2	4	12489	a6D	3/2	4	1241	11248	2.80e-03	7.32e+04
1.298	a4D	3/2	4	12489	a6D	1/2	2	1406	11083	1.23e-03	7.32e+04
1.600	a4D	3/2	4	12489	a4F	7/2	8	3496	8993	4.03e-03	7.32e+04
1.712	a4D	3/2	4	12489	a4F	5/2	6	4083	8406	1.13e-03	7.32e+04
1.798	a4D	3/2	4	12489	a4F	3/2	4	4485	8004	2.00e-03	7.32e+04
1.271	a4D	1/2	2	12729	a6D	1/2	2	1406	11323	3.82e-03	4.34e+04
1.664	a4D	1/2	2	12729	a4F	5/2	6	4083	8645	4.56e-03	4.34e+04

Table A.1: Spectroscopic properties of [Fe II] lines observed in TMC1A. Critical densities (n_{crit}) for the Cloudy excitation model are calculated using Einstein A-coefficients and collisional strengths from Verner et al. (1999), evaluated at $T = 7000$ K for consistency with previous shock studies (e.g., Koo et al. 2016). The critical density is defined as $n_{\text{crit}} = \sum A_{ki} / \sum C_{ki}$, where A_{ki} is the spontaneous emission rate and $C_{ki} = \beta \Omega_{ki}(T) / (g_k \sqrt{T})$ is the collisional de-excitation rate. Here, $\Omega_{ki}(T)$ is the collision strength, g_k the statistical weight of the upper level, and $\beta = 8.63 \times 10^{-6}$ a constant. The sums run over all radiative ($k > i$) and collisional ($k \neq i$) transitions from level k .

λ (μm)	I (B)	I (F1)	I (F2)	I (F3)	R (B)	R (1)	R (2)	R (3)
25.988	1.85e-02	1.80e-02	1.28e-02	9.22e-03	1.058	2.558	7.668	4.471
5.340	2.06e-02	1.39e-02	8.21e-03	1.45e-02	1.177	1.976	4.904	7.016
17.936	3.26e-02	2.48e-02	1.04e-02	9.04e-03	1.867	3.517	6.225	4.384
24.519	1.21e-02	6.36e-03	3.29e-03	1.60e-03	0.694	0.904	1.968	0.776
1.257	3.14e-03	1.20e-03	3.17e-04	4.75e-04	0.180	0.171	0.189	0.231
1.321	1.51e-03	6.20e-04	1.77e-04	2.13e-04	0.087	0.088	0.106	0.103
1.372	1.18e-03	5.17e-04	1.26e-04	1.61e-04	0.068	0.073	0.075	0.078
1.644	1.75e-02	7.04e-03	1.67e-03	2.06e-03	1.000	1.000	1.000	1.000
1.810	5.53e-03	2.16e-03	5.28e-04	6.12e-04	0.317	0.307	0.315	0.297
1.295	—	—	—	8.00e-05	—	—	—	0.039
1.328	6.53e-04	2.55e-04	5.16e-05	6.51e-05	0.037	0.036	0.031	0.032
1.534	3.47e-03	1.23e-03	2.34e-04	2.56e-04	0.199	0.174	0.140	0.124
1.677	4.11e-03	1.44e-03	2.63e-04	2.52e-04	0.235	0.204	0.157	0.122
1.801	4.09e-03	1.36e-03	2.53e-04	2.64e-04	0.234	0.193	0.151	0.128
1.279	7.10e-04	2.57e-04	5.26e-05	4.42e-05	0.041	0.037	0.031	0.021
1.298	2.89e-04	1.06e-04	1.47e-05	2.30e-05	0.017	0.015	0.009	0.011
1.600	3.44e-03	1.17e-03	2.25e-04	2.10e-04	0.197	0.166	0.135	0.102
1.712	1.20e-03	4.13e-04	8.20e-05	6.21e-05	0.069	0.059	0.049	0.030
1.798	2.92e-03	9.44e-04	1.74e-04	—	0.167	0.134	0.104	—
1.271	4.00e-04	1.59e-04	2.66e-05	2.27e-05	0.023	0.023	0.016	0.011
1.664	2.23e-03	7.77e-04	1.49e-04	1.53e-04	0.128	0.110	0.089	0.074

Table A.2: Continuum-subtracted integrated intensities of [Fe II] lines observed at distinct jet locations. The first column is the rest-wavelength taken from NIST, then the 4 columns marked "I" represent the observed intensity at 4 distinct locations (in $\text{ergs/cm}^2/\text{s/sr}$) with an aperture of $0.7''$. The columns marked "R" represent the ratio of that line with the $1.644 \mu\text{m}$ line. Missing data (—) is due to cases where artifacts (see Sec. 2) exist in the aperture (e.g. 1.295 , $1.798 \mu\text{m}$ lines).

	B	F1	F2	F3
Observed $I_{1.257}/I_{1.644}$	0.18	0.17	0.19	0.23
C89, $R_V=5.5$	3.78 / 17.59	3.88 / 18.08	3.68 / 17.12	3.28 / 15.27
C89, $R_V=3.1$	3.78 / 20.82	3.88 / 21.39	3.68 / 20.27	3.28 / 18.07
WD01, $R_V=3.1$	4.73 / 18.12	4.86 / 18.63	4.60 / 17.64	4.10 / 15.73
WD01, $R_V=5.5$	4.79 / 18.15	4.92 / 18.66	4.66 / 17.67	4.16 / 15.76
KP5	4.58 / 18.12	4.71 / 18.62	4.46 / 17.64	3.98 / 15.73
Gordon, $R_V=3.1$	3.57 / 22.22	3.67 / 22.84	3.48 / 21.63	3.10 / 19.29
Gordon, $R_V=5.5$	3.57 / 23.36	3.67 / 24.01	3.48 / 22.74	3.10 / 20.28
Mean $A_\lambda \pm \text{Std Dev}$	4.11 ± 0.52	4.23 ± 0.53	4.00 ± 0.50	3.57 ± 0.45
Mean $A_V \pm \text{Std Dev}$	19.77 ± 2.17	20.32 ± 2.23	19.25 ± 2.11	17.16 ± 1.88

Table A.3: Observed [Fe II] $1.257/1.644$ intensity ratios and the corresponding extinction values ($A_{1.644}$ and A_V) derived toward each jet location analyzed in this study (see Fig. 1), calculated using various extinction curves (see caption of Fig. 2) and an intrinsic ratio of 1.18 taken from the atomic dataset used in the Cloudy model (see Sect. 3). The top row lists the observed line ratios used to infer extinction, followed by extinction values derived from each extinction law, formatted as $A_{1.644} / A_V$. The bottom two rows show the mean and standard deviation of $A_{1.644}$ and A_V across all extinction laws for each location. The mean $A_{1.644}$ value is used to normalize the extinction differences ΔA_λ , yielding $\beta_\lambda = A_\lambda / A_{1.644}$ in Section 4. The A_V values are included to illustrate that differences in R_V across extinction laws—specifically where both $R_V = 3.1$ and $R_V = 5.5$ are considered—have a smaller effect on near-IR extinction ($A_{1.644}$) compared to optical extinction (A_V).

λ	$R_{corrected}$				\bar{n}_e			
	B	F1	F2	F3	B	F1	F2	F3
1.295	0.338	0.720	1.407	0.161	—	—	—	$0.8^{1.5}_{0.5}$
1.328	0.158	0.159	0.125	0.110	$4.7^{90.0}_{2.0}$	$5.0^{90.0}_{2.0}$	$2.0^{3.5}_{1.0}$	$1.4^{2.0}_{0.8}$
1.534	0.301	0.268	0.210	0.178	$3.7^{20.0}_{2.0}$	$2.4^{5.0}_{1.5}$	$1.1^{2.0}_{0.7}$	$0.8^{1.0}_{0.5}$
1.677	0.209	0.181	0.140	0.110	$3.1^{8.5}_{1.5}$	$2.0^{3.5}_{1.0}$	$0.9^{1.5}_{0.6}$	$0.5^{0.8}_{0.3}$
1.801	0.143	0.116	0.093	0.083	$3.3^{10.0}_{1.5}$	$1.7^{3.0}_{0.9}$	$0.9^{1.5}_{0.5}$	$0.7^{1.0}_{0.4}$
1.279	0.230	0.217	0.170	0.097	$6.8^{100.0}_{3.5}$	$5.1^{90.0}_{2.5}$	$2.4^{3.5}_{1.0}$	$0.7^{1.0}_{0.5}$
1.298	0.084	0.080	0.043	0.046	$3.3^{9.5}_{2.0}$	$2.9^{6.5}_{1.5}$	$0.8^{1.5}_{0.5}$	$0.9^{1.0}_{0.6}$
1.600	0.229	0.194	0.156	0.116	$3.6^{10.0}_{2.0}$	$2.4^{3.5}_{1.5}$	$1.5^{2.0}_{0.9}$	$0.8^{1.0}_{0.6}$
1.712	0.055	0.047	0.039	0.025	$2.8^{5.0}_{1.5}$	$2.0^{3.0}_{1.0}$	$1.4^{2.0}_{0.9}$	$0.6^{0.8}_{0.4}$
1.798	0.102	0.081	0.065	0.116	$3.7^{20.0}_{2.0}$	$2.0^{3.0}_{1.0}$	$1.2^{2.0}_{0.8}$	—
1.271	0.137	0.142	0.091	0.052	$4.0^{20.0}_{2.5}$	$4.6^{85.0}_{2.5}$	$1.5^{2.0}_{1.0}$	$0.6^{0.8}_{0.4}$
1.664	0.119	0.103	0.083	0.070	$3.5^{9.5}_{2.0}$	$2.3^{3.5}_{1.5}$	$1.5^{2.0}_{1.0}$	$1.0^{1.5}_{0.7}$
Average n_e					$3.6\text{e}+04 \pm 1\text{e}+04$	$2.5\text{e}+04 \pm 0.6\text{e}+04$	$1.5 \pm 5\text{e}+03$	$8.0\text{e}+03 \pm 3\text{e}+03$

Table A.4: Estimated electron densities calculated using the ‘a4D’ line intensity ratios relative to the 1.644 μm line. The extinction magnitude is calculated for each extinction curve, and each curve is used to correct for extinction at each line’s wavelength. This process yields a range of corrected line ratios, with deviations on the order of 10^{-3} due to differences among the extinction curves. The reported standard deviation for the electron density accounts for both the variation among corrected line ratios for each extinction curve and the variation in electron densities matched to the model at each temperature ($T = 5 \times 10^3 - 2 \times 10^4$ K). The final row shows the weighted average electron density and its weighted standard deviation. The results reveal a consistent trend of decreasing electron density with increasing distance from the jet.